iScience

CellPress
OPEN ACCESS

Article

Penetrating the ultra-tough yeast cell wall with finite element analysis model-aided design of microtools

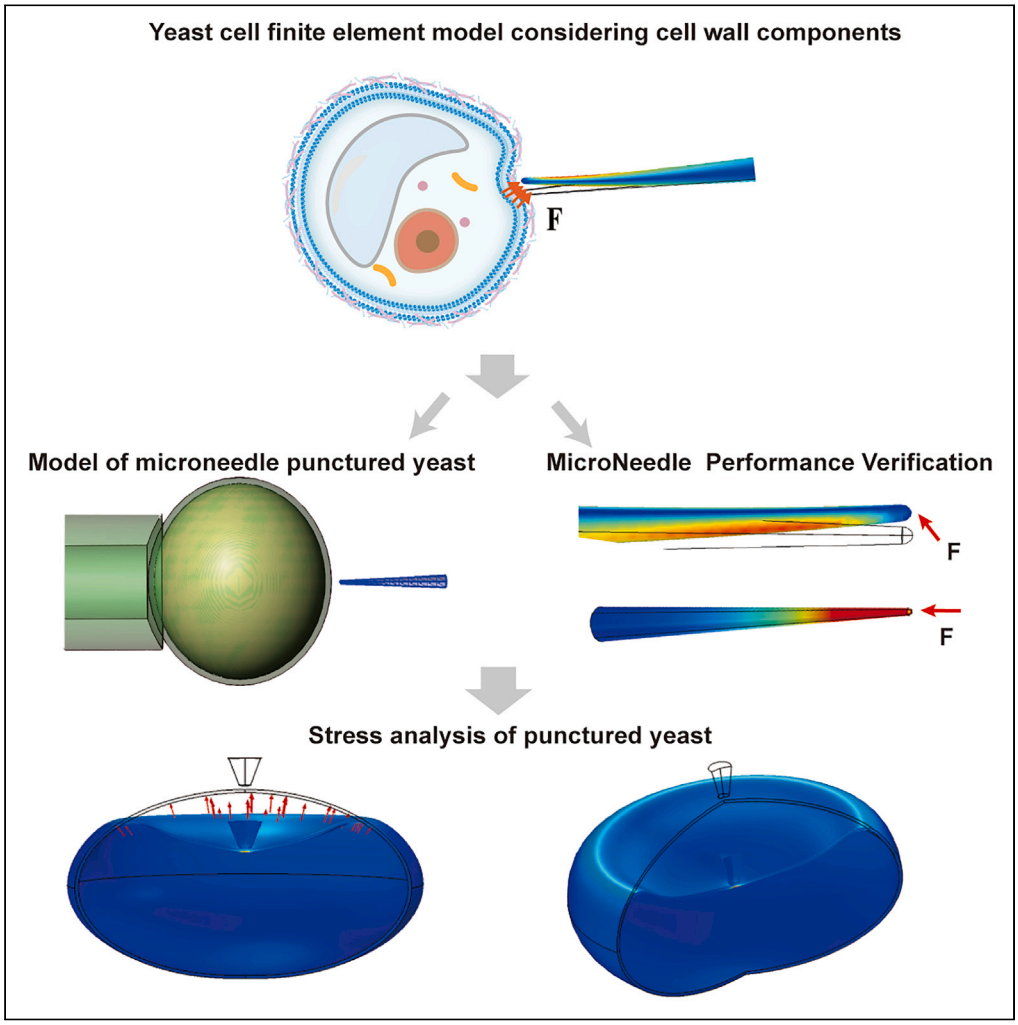

Yanfei Zhang, Wende He, Li Wang, Weiguang Su, Hao Chen, Anqing Li, Jun Chen

chenjun@qlu.edu.cn

Highlights

Proposed an FEA model for penetrating the yeast during microinjection

Optimized the microneedle profile for minimum bending due to injection offset

Provided guidelines for minimized damage to the yeast cells during microinjection

Zhang et al., iScience *27*, 109503
April 19, 2024 © 2024 The Authors. Published by Elsevier Inc.
https://doi.org/10.1016/j.isci.2024.109503

iScience

CellPress
OPEN ACCESS

Article

Penetrating the ultra-tough yeast cell wall with finite element analysis model-aided design of microtools

Yanfei Zhang,[1,2] Wende He,[1,2] Li Wang,[1,2] Weiguang Su,[1,2] Hao Chen,[1,2] Anqing Li,[1,2] and Jun Chen[1,2,3,*]

SUMMARY

Microinjecting yeast cells has been challenging for decades with no significant breakthrough due to the ultra-tough cell wall and low stiffness of the traditional injector tip at the micro-scale. Penetrating this protection wall is the key step for artificially bringing foreign substance into the yeast. In this paper, a yeast cell model was built by using finite element analysis (FEA) method to analyze the penetrating process. The key parameters of the yeast cell wall in the model (the Young's modulus, the shear modulus, and the Lame constant) were calibrated according to a general nanoindentation experiment. Then by employing the calibrated model, the injection parameters were optimized to minimize the cell damage (the maximum cell deformation at the critical stress of the cell wall). Key guidelines were suggested for penetrating the cell wall during microinjection.

INTRODUCTION

Yeast is widely adopted as a cell factory for fermentation in various industries such as food preparation, the ethyl alcohol industry, pharmaceutical production (e.g., opioids[1,2] and protein drugs[3]), green fuel production (like ethanol),[4,5] and more. It is also a commonly used model in eukaryotic biology research.[6,7] Genetic engineering researchers tried to introduce foreign substances (like artificially modified exogenous genes) into the host yeast cells to change their functionalities.[8] Traditional methods for introducing foreign substances into individual target cells encompass biological, chemical, and physical approaches.[9,10] Biological methods often involve virus-mediated transfection, with viral vectors being widely utilized in gene therapy due to their high efficiency, specificity, and simplicity. This approach has demonstrated successful clinical results.[11,12] However, viral vectors can only modify specific cell types, which are immunogenic and cytotoxic.[13] In addition, the extraneous viral vector may lead to genomic mutations and give undesirable results.[14]

The principle of the chemical method is that positively charged chemicals (like cationic polymer (DEAE-dextran,[15] chitosan[16]), calcium phosphate,[17] cationic liposomes (CLs),[18] etc.) can be combined to the negatively charged cell membrane and finally flow into the cell. Due to the cell wall barrier, these commonly used chemicals are blocked from combining with the cell membrane, thus cannot enter yeast cells.

Common physical methods include electroporation,[19] laser,[20] gene gun,[21] and microinjection.[22] Electroporation can create temporary pores in cell membranes by applying a short electrical pulse, which allows foreign substances pass into cells.[23] Laser-mediated transfection uses a pulse laser to irradiate a cell membrane to form a transient pore.[17] However, the problems of the electroporation and laser methods is that a significant proportion of the cells may be destroyed.[24] The "gene gun" method has been successfully applied to many crops (corn, wheat). However, it is not suitable for yeast cells because the commonly used bullet particles (about 4 μm) in the "gene gun" method are too large for yeast cells (about 8 μm) and can cause serious damage to the yeast cells.[25] Accordingly, these traditional transfection methods are not suitable for yeast cells.

Modern genetic engineering for yeast requires an efficient and precise way of introducing foreign substances (like artificially modified exogenous genes) into the host yeast cells.[8] Microinjection has attracted much attention with the development of micro-fabrication and micro-robotics in recent years. Due to the advantages of non-toxicity and high controllability, microinjection of animal cells has been widely adopted in clinical trials and research labs.[26] Current microinjection methods mainly include direct injection,[27] piezo-driven,[28,29] micro-drill,[30] and microfluidic.[31] Penetrating the soft animal cell membrane or yolk membrane has been solved by using a sharp micropipette or a piezo-driven micropipette. However, for cells protected by the cell wall structure, like yeast, traditional microinjection is still inapplicable due to the ultra-tough cell wall.

The first challenge in microinjection of yeast is to break the ultra-tough yeast cell wall. This is mainly because the microstructure of yeast cell wall is a complex combination of dextran, mannan, and chitin which are firmly connected with each other by covalent bonds to form a

[1]School of Mechanical Engineering, Qilu University of Technology (Shandong Academy of Sciences), Jinan 250353, China
[2]Shandong Institute of Mechanical Design and Research, Jinan 250353, China
[3]Lead contact
*Correspondence: chenjun@qlu.edu.cn
https://doi.org/10.1016/j.isci.2024.109503

This is an open access article under the CC BY-NC-ND license (http://creativecommons.org/licenses/by-nc-nd/4.0/).

strong spiral fiber.[32] The turgor cell pressure supports the cell wall from inside, which makes the cell wall more rigid.[33] At the scale of micrometer, the stiffness of the yeast cell wall could be greater than that of the traditional sharp microinjection needles. This can lead to significant bending or even breaking down on the sharp tip. Blunt microneedles are less likely to bend but may cause too much damage to yeast cells and lead to a low survival rate after injection. In addition, it is difficult to break the cell wall directly through a single shot due to the tenacity of the yeast cell wall. A piezo-impact micromanipulator was used to drive a flexible glass pipette to grind the yeast cell wall repeatedly.[34] It took about 12 min to break the yeast cell wall, which was much longer than injecting animal cells (about 1 s for adherent cell injection[35]). Accordingly, penetrating the yeast cell wall is much more difficult than that of the animal cell membrane in traditional microinjections.

In recent years, finite element analysis (FEA) modeling the yeast cell and the penetration process was applied to study the mechanical behavior of the target cell. The mechanical parameters during microinjection (e.g., internal cellular strains and stresses) can be calculated from the model, which is difficult to measure directly by experiments.[36,37] These parameters can be used to explore deformations of the target cell, which can be used to describe cell damage.

Existing yeast models mainly include tensegrity model,[38] percolation model,[39] elastic model,[40] poroelastic model,[41] and Power-law rheology.[42] Based on these empirical models sever biological methods are often al 2D and 3D models were constructed. For example, epithelial cells,[43] endothelial cells,[44] adipocyte cells,[45] and adherent cells.[46] Existing models are mainly used to analyze animal cells without cell wall. They are not suitable for analyzing the penetration process of yeast cells.

In this paper, a multilayer yeast cell model was proposed as a three-layer ellipsoid axis-symmetric structure. The Neo-Hookean superelastic fiber and the glycoprotein interweaving structure in the yeast cell wall were modeled into an external layer. The mechanical functions of the cytoplasm and organelles inside the cell are modeled as the internal turgor pressure. The key parameters of yeast cell wall in the model (the Young's modulus, the shear modulus, and the Lame constant) were calibrated from nanoindentation experiments. The calibrated yeast cell model was employed to explore the effects of the microneedle parameters (tip radius, needle wall angle, and length) during penetration. The process of penetration is simulated by FEA method to obtain the distributions of the stress and strain of the cell and the needle during microinjection. By optimizing the needle shape and injection angle, a feasible microinjection strategy was provided for penetrating the yeast cell wall with minimal damage to the cell.

RESULTS AND DISCUSSION

Model for yeast cells

In our study, we employed the solid mechanics module in COMSOL Multiphysics (6.0) (a trial version) to create a 2D axisymmetric model to study the yeast cell structures. The mechanical strength of the yeast cell wall (Figure 1A) is attributed to mannan, β1, 3-glucan, and chitin. The thickness of the cell wall in the model was set to 0.3 μm based on a consistent thickness-to-radius ratio of 0.037 as reported in literature.[45] The peripheral endoplasmic reticulum forms a dynamic network inside the yeast cell, playing a significant role in contributing to membrane curvature.[47] In our model, we equate various organelles to cytoplasmic effects and utilize the internal turgor pressure of the cell wall instead (Figure 1E). The phospholipids in cell membranes exhibit nuanced mechanical behaviors, including bending, stretching, and compression, responding nonlinearly to elevated strains.[48] Our model includes a bending energy model to illustrate membrane bending behavior,[49,50] complemented by a nonlinear material model to capture nonlinearity attributed to cellular expansion pressure (Equations 19, 20, 21, 22, 23, 24, 25, 26, 27, and 28). We guarantee convergence and stability of the solution to the energy minimization problem through the utilization of nonlinear solvers and adaptive grid methods within the decoupling strategy, employing distinct solving methodologies. We investigated the stress on cells undergoing changes in turgor pressure without external force (Figures S3A and S3B). The stretch resistance of the yeast cell wall and the inextensible nature of local surfaces play pivotal roles in influencing cell morphology and its capacity to withstand external forces. The wall's malleability correlates with turgor pressure, where higher pressure increases its ductility. Successful puncturing hinges on the puncture force surpassing the cell wall's threshold pressure, necessitating considerations of both stiffness and cutting force. The yeast cell membrane requires a rigid structure, nonlinear surface forces, and resistance to deformation. In contrast, the fluid biofilm is inherently prone to stretching and deforming easily. Modeling fluid biofilms leans toward simpler fluid mechanics principles due to their distinct characteristics. Variations in yeast membrane properties significantly impact microinjection ease, facilitating an exploration of the behavior of injected material within cells.

The study of material models in cell mechanics has progressed through several stages, encompassing linear elastic models,[51,52] elastoplastic models,[53] and hyperplastic models.[54] The Neo-Hookean hyperplastic model is chosen for its precise representation of the mechanical behavior of the yeast cell wall. This model adeptly captures the nonlinear elasticity observed in the cell wall, closely mimicking its responses under various stress conditions. Balancing simplicity with accuracy, the model has been validated by experiments, effectively predicting yeast cell mechanics within specific stress ranges. In hyperplastic materials, the constitutive relations depend on a strain energy density function associated with the deformation gradient. Typically, expressions for strain energy density and stress are formulated in terms of the compression ratio (λ), representing the extent of deformation. The stretch ratio, defined as $\lambda = h/h_0$ (where h is the deformed length and h0 is the original length), holds a central role in these relationships. In our model, the yeast cell wall is conceptualized as a hyperplastic shell, incorporating two considerations. The initial model focuses solely on the mechanical effects of dextran interweaving within the cell wall, with a defined thickness (h) of 0.3 μm. Subsequently, in the second model, we incorporate the influence of glycoprotein cross-links while maintaining the thickness unchanged. Both models regard the cell wall shell as a material resilient to tension, bending, and shear.

CellPress
OPEN ACCESS

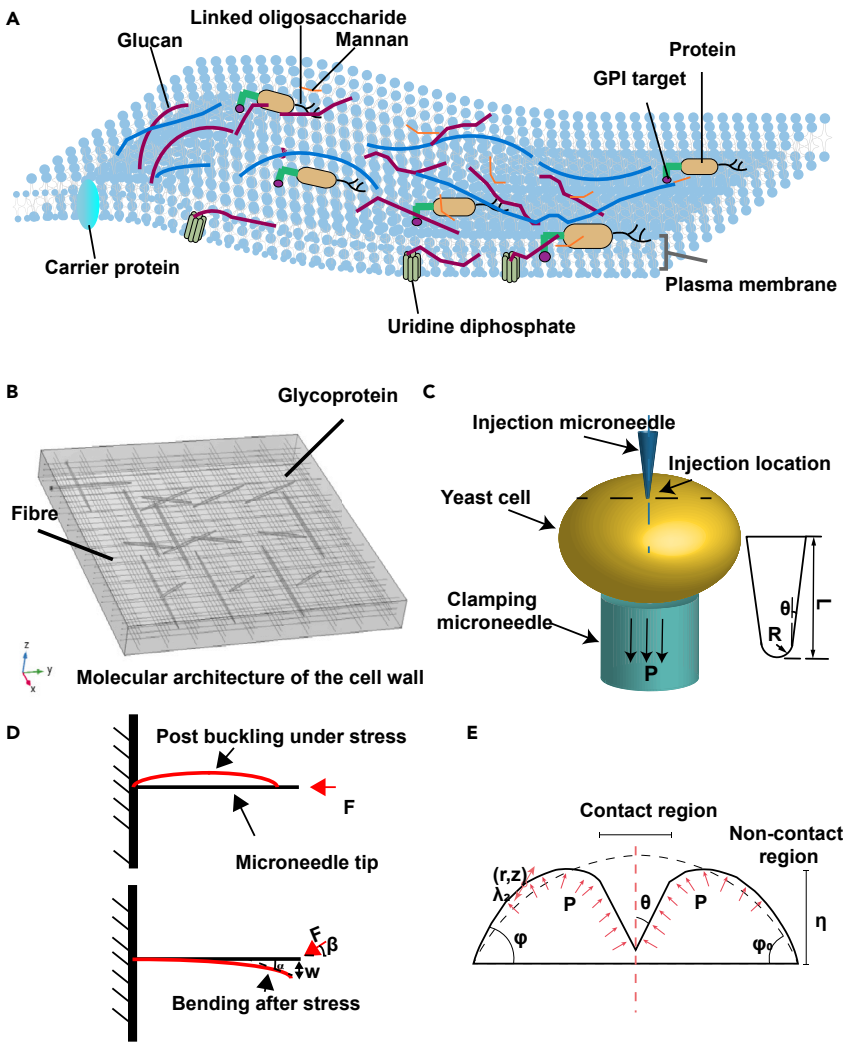

Figure 1. Construction of yeast cell model based on cell structures and puncture model

(A) The composition of the yeast cell wall (B) Cell wall model constructed by crosslinking glycoproteins with fibers.

(C) The FEA model for microinjection of a yeast cell (8 μm major axis and 6 μm minor axis). Tip radius (R), tip length (L), and taper angle (θ) of the injection needle is defined in the sketch.

(D) The simplified cantilever beam model of the pin-tip by applying axial force and bending force, respectively.

(E) Cross-section view of the yeast cell during puncture.

We consider using a bending energy model to describe the bending behavior of the membrane and combine it with a nonlinear material model to explain its nonlinearity, which is related to the cell expansion pressure P, and the formula is as follows.

$$E = \int \left(k_c H^2 + \gamma - \lambda \left(1 - \frac{1}{2} \nabla \cdot n \right) \right) dA + P \int dV, \quad \text{(Equation 1)}$$

Here E is the total bending elastic energy of the membrane, k_c is the bending modulus of the membrane, H is the average curvature of the membrane, $\lambda\left(1 - \frac{1}{2}\nabla \cdot n\right)$ represents the effect of surface tension field, and γ is surface tension, where $\frac{1}{2}\nabla \cdot n$ represents the deformation rate of the membrane and λ is the Lagrange multiplier used to maintain the local non-expandability of the membrane.

The bending energy density of the membrane is related to the curvature and deformation of the cell membrane and can be expressed by the energy density function W as:

$$W = \frac{1}{2} k_c \int \frac{(k1+k2+k3)^2}{4} dA, \quad \text{(Equation 2)}$$

Here k1, k2, and k3 are the principal curvatures of the ellipsoid and can be expressed as the metric tensor g in the ellipsoid coordinate system and calculated in the basic form I:

$$g = \begin{bmatrix} E & F \\ F & G \end{bmatrix}, \quad \text{(Equation 3)}$$

$$I = \begin{bmatrix} E & F & 0 \\ F & G & 0 \\ 0 & 0 & 1 \end{bmatrix}, \quad \text{(Equation 4)}$$

Here,

$$E = r_\xi r_\xi = a^2 \sin^2 \xi \sin^2 \eta + b^2 \cos^2 \xi \sin^2 \eta \quad \text{(Equation 5)}$$

$$F = r_\xi r_\eta = 0, \quad \text{(Equation 6)}$$

$$G = r_\eta r_\eta = a^2 \cos^2 \xi \cos^2 \eta + b^2 \sin^2 \xi \cos^2 \eta + c^2 \sin^2 \eta, \quad \text{(Equation 7)}$$

Here r_ξ and r_η are the parametric equations of the ellipsoid surface respectively, ξ, η are parameters in the ellipsoid coordinate system, a, b, and c are the semi-axis lengths of the ellipsoid on the three coordinate axes and b = c. Cell pressure can be expressed as:

$$P = k\frac{dF}{dL}, \quad \text{(Equation 8)}$$

K is the curvature of the ellipsoid, expressed as k = 1/ab. The relationship between the force F on the inner surface and the turgor pressure is related to the surface area A, expressed as,

$$F = PA, \quad \text{(Equation 9)}$$

$$A = \frac{4\pi}{3}(ab + ac + bc), \quad \text{(Equation 10)}$$

Here a = 4 μm, b = c = 3 μm, the inner surface area Ain can be approximated by the surface area of the ellipsoid minus the thickness h_0:

$$A_{in} = A - 4\pi abh_0, \quad \text{(Equation 11)}$$

In the absence of external force, if the cell volume remains unchanged, the relationship between cellular pressure and internal surface pressure is linear. Studies have shown that when turgor pressure increases, cell volume increases, and is related to the bending modulus of the cell membrane and the elastic modulus of the cell wall, making it a linear relationship. We explored the stress on cells that change turgor pressure without external force (Figures S4A and S4B). The fitting relationship equation between external force and cell turgor pressure are as follows, and their values are in Table 1.

$$y = Ae^{\frac{-x}{t1}} + y_0, \quad \text{(Equation 12)}$$

The fitting equation without external force are as follows, and their values are in Table 2.

$$y = y_0 + \left(\frac{A}{w\sqrt{\frac{\pi}{2}}}\right) e^{\left(\frac{-2(x-x_c)}{w}\right)^2}, \quad \text{(Equation 13)}$$

We use the X = x (X, 0) coordinate to represent the original position of the material at the contact location between the microneedle and the cell wall, which is called the material coordinate system. After microneedle puncture, the location will move to the new position x = x (X, t). Both sets of coordinates take the center of the 2D yeast cell model as the origin and have the same direction. The spatial coordinate system vector $x = x_1\widehat{n_1} + x_2\widehat{n_2}$, where $(\widehat{n_1}, \widehat{n_2})$ are two-unit orthogonal vectors on the cell wall surface. Material coordinate system $X = X_1\widehat{n_1} + X_2\widehat{n_2}$. The displacement vector of the contact location u = x (x, t) and the deformation gradient of X projected on the surface is

$$F = I + \nabla u, \quad \text{(Equation 14)}$$

where I is the two-dimensional identity tensor, and the plane Euler strain tensor and Lagrangian strain tensor are respectively

$$e = \frac{1}{2}(I - B^{-1}), \quad \text{(Equation 15)}$$

CellPress
OPEN ACCESS

Table 1. Parameters of the relationship curve between external force and turgor pressure

A	y_0	t_1	R^2
− 7.22± 1.55	7.74±1.63	256.98±86.24	0.989

$$E = \frac{1}{2}(C - I), \quad \text{(Equation 16)}$$

Here $B = FF^T$ and $C = F^TF$ are the left and right Cauchy-Green tensors projected on the surface respectively.

$$e \approx E \approx \epsilon = \frac{1}{2}\left[\nabla u + (\nabla u)^T\right], \quad \text{(Equation 17)}$$

where ϵ , e, E are the second-order tensors in two-dimensional space, the Cauchy surface stress tensor and the Piola-Kirchhoff stress tensor. The strain tensor is composed of the in-plane terms of the corresponding three-dimensional strain tensor projected on the surface. In three-dimensional space, the strain energy density is

$$\Psi = \Psi(I_1 + I_2 + I_3), \quad \text{(Equation 18)}$$

The strain energy density function of Neo-Hookean incompressible materials is expressed as

$$Ws = \frac{1}{2}\mu(I_1 - 3) - \mu \ln J_{el} + \frac{1}{2}\lambda(\ln J_{el})^2, \quad \text{(Equation 19)}$$

The first Piola-Kirchhoff stress tensor S and the Cauchy stress tensor T can be expressed as functions of the second Piola-Kirchhoff stress tensor:

$$S = JF^{-1}TF^{-T}, \quad \text{(Equation 20)}$$

where F is the deformation gradient, J is the volume ratio, J = w1w2 = 1. The 2PK stress tensor can also be expressed by the in-plane diagonal stress σ^0, where p is the Lagrange multiplier,

$$S = \sigma^0 + \mu I - pC^{-1}, \quad \text{(Equation 21)}$$

When converting an incompressible hyperelastic surface into an equivalent Neo-Hookean incompressible shell. Consider biaxial stretching with in-plane initial pressure, the deformation gradient of which is,

$$F = \begin{bmatrix} w_1 & 0 & 0 \\ 0 & w_2 & 0 \\ 0 & 0 & 1/(w_1 w_2)^2 \end{bmatrix}, \quad \text{(Equation 22)}$$

Here, w_1 and w_2 are the main tensions in the plane, and the Cauchy stress tensor is derived in vector form

$$\begin{bmatrix} T_{11} \\ T_{22} \\ T_{33} \end{bmatrix} = \begin{bmatrix} \sigma^0 w_1{}^2 \\ \sigma^0 w_2{}^2 \\ 0 \end{bmatrix} + \begin{bmatrix} \mu w_1{}^2 \\ \mu w_2{}^2 \\ \mu/(\mu w_1{}^2 w_2{}^2) \end{bmatrix} - \begin{bmatrix} p \\ p \\ p \end{bmatrix}, \quad \text{(Equation 23)}$$

The constraints of the equivalent shell are

$$T_{33} = 0, \quad \text{(Equation 24)}$$

The following formula can be obtained,

$$p = \mu / (w_1{}^2 w_2{}^2), \quad \text{(Equation 25)}$$

$$\begin{bmatrix} T_{11} \\ T_{22} \\ 0 \end{bmatrix} = \begin{bmatrix} \sigma^0 w_1{}^2 + (w_1{}^2 - 1)\mu \\ \sigma^0 w_2{}^2 + (w_2{}^2 - 1)\mu \\ 0 \end{bmatrix}, \quad \text{(Equation 26)}$$

Establish the relationship between hyperplastic strain and displacement,

$$\varepsilon_x = \frac{\partial u}{\partial x} + \frac{1}{2}\left[\left(\frac{\partial u}{\partial x}\right)^2 + \left(\frac{\partial v}{\partial x}\right)^2 + \left(\frac{\partial w}{\partial x}\right)^2\right], \quad \text{(Equation 27)}$$

Table 2. Parameters of turgor pressure curve without external force

y_0	x_c	w	A	R^2
− 46.22 ± 39.98	7.96 ± 27.79	4.83 ± 10.10	64704.15 ± 1172687.69	0.99937

The shear strain is formulated as,

$$\gamma_{xy} = \frac{\partial u}{\partial y} + \frac{\partial v}{\partial x} + \frac{\partial u}{\partial y}\frac{\partial u}{\partial x} + \frac{\partial v}{\partial x}\frac{\partial v}{\partial y} + \frac{\partial w}{\partial y}\frac{\partial w}{\partial x}, \quad \text{(Equation 28)}$$

The yeast cell model consists of the Young's modulus, the shear modulus, and the hyperplastic material parameters.

Model calibration

The force-displacement curve, as depicted in the indentation curve (Figure 2C), characterizes the force necessary to penetrate the yeast cell to a specific depth.[55] This curve's morphology is contingent not solely upon the elastic properties of the sample but also on the tip's geometric configuration. Utilizing this curve, we fit a model Equation 33 to derive the coefficients ($a = 0.0121 \pm 0.00069, b = -0.239 \pm 0.015, c = 1.659 \pm 0.159, d = 2.165 \pm 0.384$) governing the puncture process. By employing a Poisson ratio (ν) of 0.48 for the cell wall material, we determined the Young's modulus (E) as 1.95 ± 0.08 MPa through curve fitting (S3). Summarizing the Young's moduli of yeast cells measured by previous researchers (Table S1), we observed variations attributed to differences in cellular environments, cell types, and cell life cycles. Moreover, the values obtained using nanoindentation measurements are significantly lower than those obtained using compression measurements by Smith. The Young's modulus we obtained by fitting is close to the nanoindentation measurement. Additionally, the shear modulus (G), obtained through Equation 16, is determined to be 0.65 ± 0.03 MPa.

In unloading conditions, yeast cells exhibit a limited ability to completely revert to their original shape due to the elastic-plastic properties of their cell wall. The experimental curve indicates that an indentation of 0.8 μm (constituting 20% of the cell's diameter) corresponds to the predetermined load threshold for cell resistance (Video S1). This threshold enables microneedles (250 μN) to pierce the cells successfully. Upon unloading to 0.2 μm, the force feedback registers zero, indicating the detachment of cells from the nanotip. This observation suggests a lack of cellular recovery post-stress, potentially arising from an irreversible rearrangement of polymer structures within the cytoplasm, in contrast to the cell wall's ability to restore its structure upon the removal of external pressure.[56] We constructed a FEA model of yeast using the fitted Young's modulus as well as the superelastic material model. In this hyperelastic material model, the Lame constant (λ) is set at 0.0005 N/m^2, and μ is 0.0002 N/m^2 (Table 3). The stress-displacement curve relationship of the model was simulated in Comsol and compared with the indentation curve obtained from the nanoindentation experiment (Figures 2A and 2D). The results indicate that the error between the indentation results of the model and the nanoindentation experiment does not exceed 10%. Furthermore, we conducted an assessment of mesh independence for the model and investigated the relationship between stress and displacement curves across varying mesh densities, namely 10,000, 20,000, 40,000, and 60,000. Our analysis revealed that with an increase in the number of meshes, the stress values exhibit oscillatory changes at constant displacements. However, as the mesh is progressively refined, the stress values tend to stabilize. Notably, the maximum error in stress values between 10,000 and 20,000 grids is approximately 6%, while the maximum error between 20,000 and 40,000 grids is around 2%. Based on these findings, it can be inferred that the numerical results have converged by this point (See Figure S5). The traditional concept of the "equivalent cone angle" is commonly applied when triangular pyramids and cone needles undergo large indentations. The Berkovich pyramid shape closely aligns with the stress concentration effect observed in cone shapes. As puncturing yeast cells fall into the category of large indentations, this model proves to be suitable for simulating and analyzing the yeast cell puncturing process.

Optimization of needle parameters

Needle shape

The critical factors influencing penetration include the tip's radius of curvature, needle wall angle, and microneedle tip radius. Theoretically, smaller radii and needle angles enhance yeast cell penetration. Simulations employing various microneedle tips within our yeast cell model revealed intriguing outcomes (Figure 3A). The von Mises stress field indicated that a 0.1 μm needle tip induced higher stress (55 MPa) compared to a nanoindentation test (25 MPa) due to stress concentration at the smaller nanoindent tip. Notably, the cone tip demanded the least displacement (0.7 μm) for cell puncture, while the spherical tip required the most (1.2 μm) (Figure 3B). While a bullet-shaped tip initially showed promise, it exhibited lower resistance to bending compared to conical and spherical tips. Considering the processing challenges associated with an oblique cone bullet tip, we ultimately opted for a conical design. Comparisons through simulations using rigid body models suggested that smaller curvatures offered superior puncture effects. However, practical considerations, including material properties such as microneedle buckling and curvature during puncture, guided our choice toward a conical tip.

Needle length

When maintaining a constant tip radius size, we varied the length of the microneedle to examine the stress-displacement relationship under different microneedle lengths. Overall image analysis (Figure 3C) indicates that, with a fixed front-end size, the effect of length on puncture

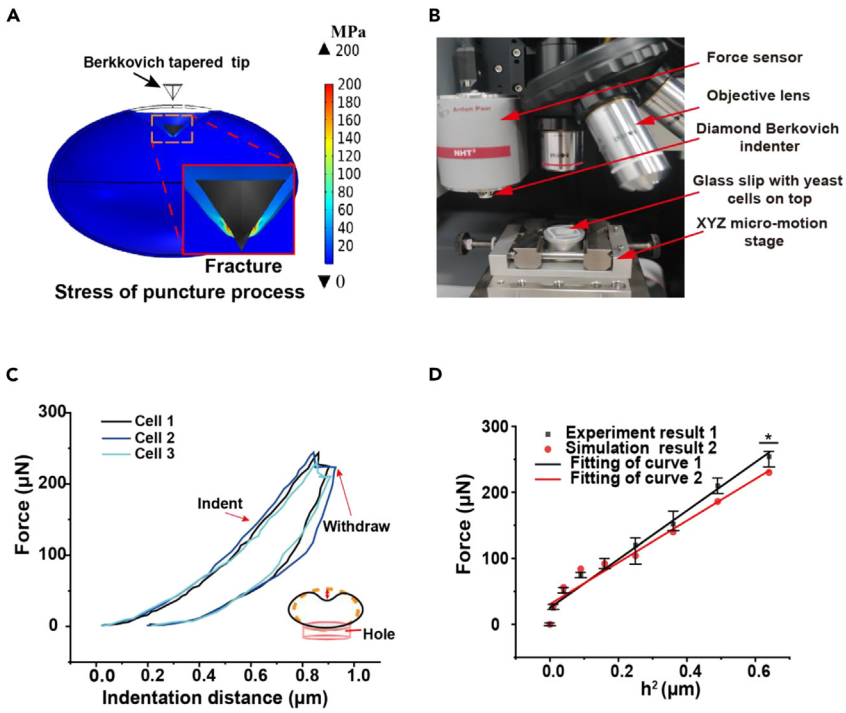

Figure 2. Model calibration

(A) FEA simulation of yeast indentation. The cell wall was penetrated when the injection force increased to 185 MPa.

(B) Setup for the nanoindentation experiments of yeast cells. Yeast cells were fixed in polycarbonate film holes and positioned on glass slides.

(C) Force-displacement curves obtained by nanoindentation experiments. The maximum indentation force was set as 250 μN.

(D) Young's modulus obtained by fitting the curve. Curve fitting was performed using Equation 16, *$p < 0.05$.

stress exhibits approximately linear growth. However, the difference in the impact of various lengths is not prominently noticeable, and the displacement at the time of puncture remains at 0.9 μm. On the contrary, the length of the microneedle influences its properties, such as its ability to resist bending. Longer microneedles are more prone to flexion and breakage. Therefore, the length of the microneedle must be carefully controlled to meet strength requirements at maximum puncture forces.

Tip radius

Exploring various tip radius sizes in constructing puncture models reveals distinctive stress levels and displacement gaps during puncture, as evident from the curves. As the tip radius increases, the stress values required for cell puncturing elevate, necessitating deeper indentation depths. Figure 3E illustrates that a 0.1 μm tip radius requires the shallowest depth for yeast cell puncturing. This phenomenon arises because smaller needle tips generate a pronounced stress concentration, facilitating the puncture process. Conversely, at a 0.4 μm radius, a notable stress increase occurs, signifying the substantial impact of needle tip radius on puncture force.

Tip contact angle

In our study, we conducted FEA simulations using a tapered needle with an arc tip (Figure 3D). Maintaining a consistent tip radius, we used this microneedle to puncture a yeast cell model, assessing force distribution along the tip. As penetration depth increased, stress at the needle-cell contact location changes, generating diverse stress fields across contact location. Notably, when aligning the tip sphere's center with the centerline, a 28° contact angle showed heightened stress levels, indicating the primary stress region during cell puncture falls within 30° of central contact surfaces. This relationship between stress and contact angles also ties to needle sharpness: sharper needles minimize cell contact, necessitating smaller angles to reach significant stress levels.

Table 3. Model parameters

cell wall thickness h (μm)	Initial stretch ratio λ_0	Young's modulus E (MPa)	initial cell turgor pressure P(MPa)	Lame constant λ (N/m2)	Lame constant μ (N/m2)
0.3	1.04	1.95 ± 0.08	0.5	0.0005	0.0002

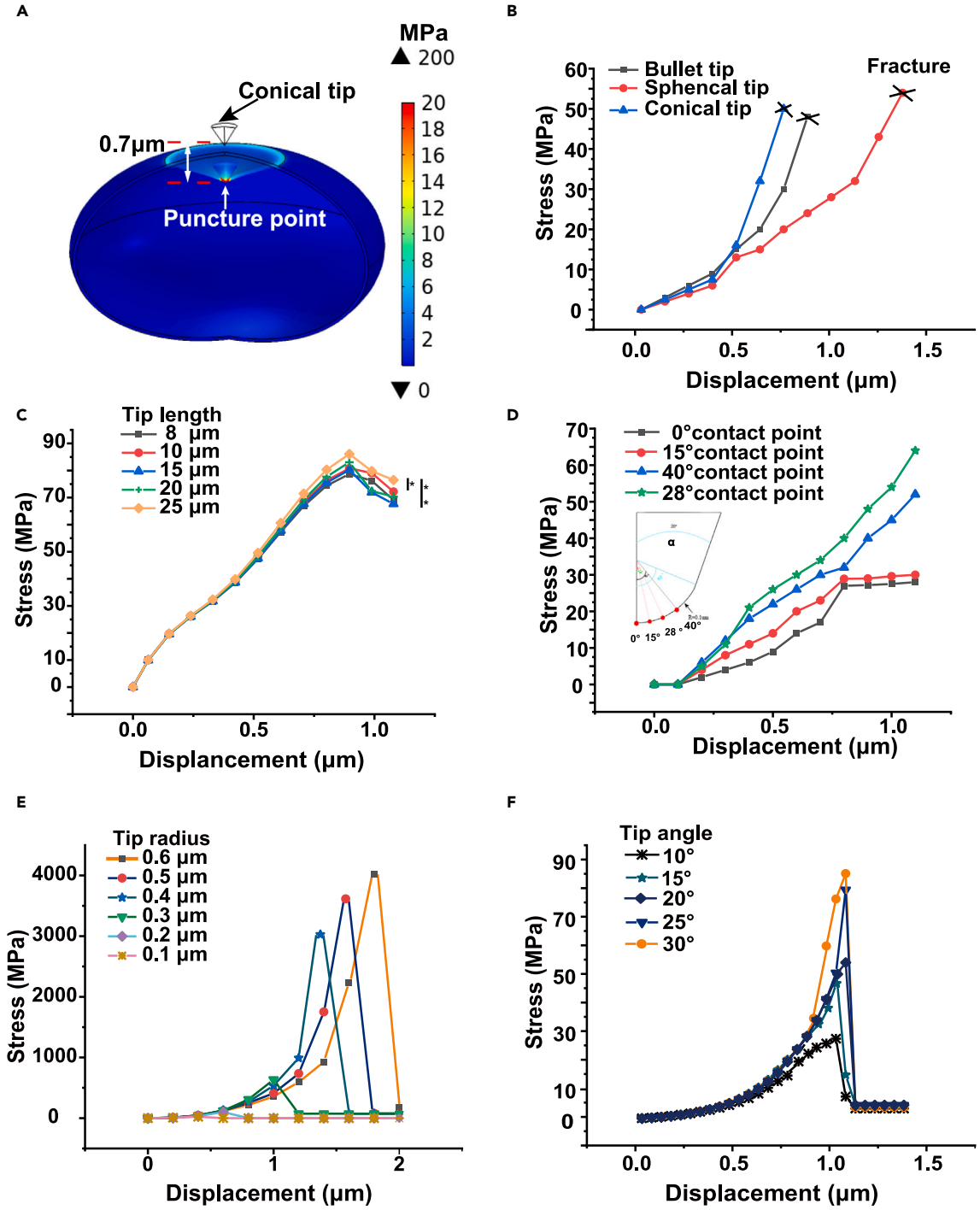

Figure 3. Analysis of stress experienced by microneedle during puncture process

(A) Stress field distribution of the yeast cell during the penetration process. Use conical to achieve cell puncture when the displacement reaches 0.7 μm, and the maximum stress on the microneedle is only 23 MPa.

(B) The stress-displacement relationship for three types of microinjector during injection. The sharper the tip of the punctured yeast cell, the smaller the desired displacement.

(C) Effect of tip on stress-displacement relationship at different microneedle lengths. When the front-end size is fixed, the effect of the simple length on the puncture stress is approximately linear growth, but the difference in the effect of different lengths is not very obvious overall.

(D) Effect of contact angles with a 0.1 μm tip radius on puncture. The 40° position location of the tip is less stress value than the 25° position location, so the main action position of the tip is within 40° or even smaller.

CellPress
OPEN ACCESS

Figure 3. *Continued*

(E) Stress-displacement relationships of puncture yeast cells with different tip radius. The spike in puncture stress growth at a tip radius of 0.4 μm indicates that the puncture force growth required is large, and if you want a small damage effect, you should choose a tip radius of 0.1–0.3 μm.

(F) Stress-displacement relationship of puncture yeast cells at different needle wall angles. The smaller the needle wall angle, the smaller the puncture force required to puncture yeast cells. The best puncture angle is 10°–15°. *$p < 0.05$, **$p < 0.01$.

Needle wall angle

While maintaining a constant tip radius of 0.2 μm, we investigated variations in the needle wall angle to assess their impact on puncture efficiency (Figure 3F). The results indicated that needle wall angles of 10° and 15° resulted in a displacement of 0.05 μm less in the punctured yeast cell model compared to other angles. Moreover, a smaller needle wall angle exerted less stress on the cell wall, facilitating easier penetration. This reduced stress is advantageous for breaking the yeast cell wall, requiring less force for puncture. In vertical penetration, for microneedle design, opting for a smaller tip radius and a reduced needle wall angle enhances cell penetration efficiency. We tentatively selected a tip radius of 0.2 μm, a needle wall angle of 10°, and a tungsten needle with a microneedle length of 40 μm. The maximum axial pressure that the microneedle can withstand at this point is calculated as 490.7 μN. However, real-world penetration processes may involve offset errors, potentially causing fine microneedle breakage due to bending stress. It's crucial to verify the strength of the selected needle parameters accordingly.

Needle bending due to offset in injection location

Calibration of the microneedle strength

During the puncturing process, deviations from the intended path create non-axial forces, leading to deflection (Figure 4A). The offset error of injection location leads to tilt contact on the cell surface. Some microneedle tips, with sizes in the nanometer range, may be too small due to their tips. As a result, the stress these microneedles can withstand during puncture falls short of the minimum stress required to penetrate yeast cells. In response to this challenge, our objective is to design microneedles capable of puncturing yeast cells while enduring non-axial stresses without breaking. Through the manipulation of the tip radius, we observed that smaller tips experience maximum strain closer to the tip. Deformation primarily takes place within 0–2 μm from the tip, with thinner tips exhibiting greater strain—a 0.1 μm tip radius showed the highest strain and extended deformation areas. Beyond a 0.5 μm tip radius, deformation predominantly concentrates at the needle tip (Figure 4B). Furthermore, maintaining the tip radius at 0.1 μm while adjusting length revealed a positive correlation between length and microneedle strain. Longer lengths resulted in increased strain and bending at the microneedle tip, especially beyond 30 μm (Figure 4C). Analyzing deflection under joint constraints of tip radius and needle wall angle reveals that deflection decreases with an increasing needle wall angle (with a constant tip radius) and increases with larger tip radii (with a constant needle wall angle) (Figure 4D). Considering our shape analysis, which favors smaller tip radii and needle wall angles for efficient yeast cell puncture, we settled on a tip radius of 0.2 μm, a 13° needle wall angle, and a 30 μm microneedle length for design parameters. Calculations estimate that these parameters can accommodate axial and transverse pressures of 872.3 μN and 74.1 μN, respectively, theoretically meeting puncture requirements while preventing excessive bending or breaking.

Puncture displacement and puncture stress required for different insertion position errors

In our investigation into microneedle injection into yeast cells, we examined the relationships between displacement, puncture stress, and the α shift angle as the microneedle shifted. In the simulation experiment with a tip radius of 0.2 μm and a microneedle length of 30 μm, we observed that minimal puncture displacement was required for vertical injection (0° offset angle), indicating minimal cell damage. As the offset angle increased, puncture displacement generally rose, suggesting that smaller offset angles cause less cell damage. However, the relationship between puncture stress and offset angle lacked a specific trend (Figure 4E). Offset angles of 10°–15° required similar puncture depths to 0° but with slightly lower puncture stress (73 MPa compared to 80 MPa at 0°). This phenomenon is related to the forces acting on the fiber model of the elliptical cell wall, where multilayered fibers facilitate better puncture at certain angles. Various angles yield diverse lateral stress distributions, necessitating distinct puncture stresses. Offset angles surpassing 45° may result in yeast cell dislodgment due to microneedle force, leading to puncture failure. Therefore, minimizing the offset angle to within 40° (preferably at 10°–15°) is crucial to ensure successful puncture while preserving cell integrity (Table 4).

Conclusion

In summary, a yeast cell model was built to analyze the penetration process for microinjection of yeast by using the FEA method. The puncture equation coefficients and the Young's modulus of the yeast cell wall were obtained by fitting the force-displacement curve from indentation by a commercial nanoindentor. The key parameters of the yeast cell wall in the cell model (the shear modulus and the Lame constant) were calibrated by this data. the profile of the microneedle was optimized (the tip radius 0.2 μm, the needle wall angle 13°, and the needle length 40 μm) to avoid breaking down the sharp needle tip in the situation of inevitable injection location offset. The optimized microneedle can break the cell wall at minimal level of cell damage (in terms of the penetration deformation on the rupture of the cell wall) during the penetration process, which was validated by the calibrated model. General guidelines on optimizing the injection parameters were suggested for microinjection of the yeast cell.

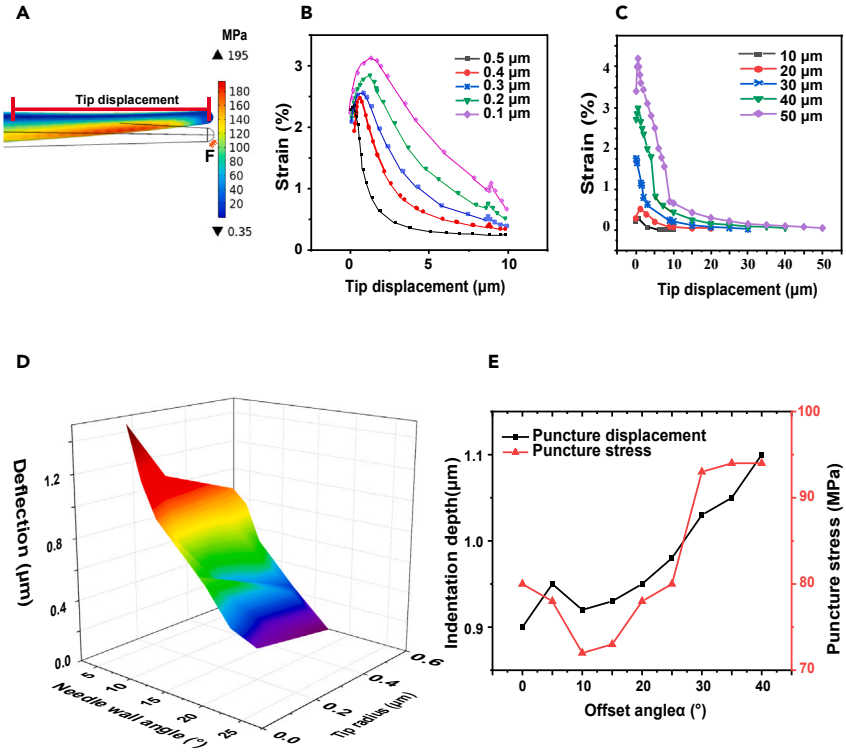

Figure 4. The effect of offset in injection location during penetration

(A) The deflection and stress distribution of the microneedle tip due to bending stress caused by offset in injection location. A maximum stress point is observed at a specific distance from the tip.

(B) The effect of tip radius on strain distribution on the microneedle. Larger tip radius lead to reduced strain generated by bending stress, concentrating higher strain levels at the tip.

(C) Strain diagram of different microneedle lengths subject to bending stress. Under identical bending stress conditions, longer microneedles generate higher strains, rendering them more susceptible to bending and breaking.

(D) The effect of the needle wall angle and the tip radius on the deflection of microneedle during injection. Greater aspect ratios of microneedles result in increased bending deviation.

(E) The effect of the insertion offset error on the puncture stress and puncture displacement. The lateral force would detach the cells to from the holding pipette when it exceeds a maximum offset angle of 45°.

Limitations of the study

A few limitations should be mentioned about our methods. First, the required penetration depth depends on the Young's modulus (E) of the target yeast cell. E varies from 0.6 MPa to 2.1 MPa according to the cell type used, culture environment, etc. In our research, the E was calibrated by nanoindentation experiment. Secondly, for the convenience of FEA simulation, the complex structures of yeast cells, such as endoplasmic reticulum, glucan, and internal organelles, were simplified into a three-layer ellipsoid axisymmetric structural model. The behaviors of these internal structures during penetration would be further studied in the future work. In addition, the yeast penetration needle is not commercially available for biologists to use like commercial glass micropipette. The required profile and dimensions of the penetration needle for certain types of yeast cells can be different. We proposed the profile design method and the fabrication method, which could help other researchers to make their own penetration tools.

STAR★METHODS

Detailed methods are provided in the online version of this paper and include the following:

- KEY RESOURCES TABLE
- RESOURCE AVAILABILITY
  - Lead contact
  - Materials availability
  - Data and code availability
- EXPERIMENTAL MODEL AND STUDY PARTICIPANT DETAILS

Table 4. Optimized parameters of in microneedle on condition of offset in injection location

Deformation area	tip radius	microneedle length	Offset angles
0–2 μm from the tip	0.2 μm	30 μm	10°–15°

- Microbe strains
- METHOD DETAILS
  - Construction of FEA models of yeast cells
  - Calibration of model parameters
  - Injection parameter modeling during penetration
  - Model construction in Comsol
  - Preparation of yeast cells
  - Calculating the cell area in optical microscopy image
  - Indentation of yeast cells
- QUANTIFICATION AND STATISTICAL ANALYSIS

SUPPLEMENTAL INFORMATION

Supplemental information can be found online at https://doi.org/10.1016/j.isci.2024.109503.

ACKNOWLEDGMENTS

The research is supported by the National Natural Science Foundation of China (no. 61901239), Taishan Scholars Program of Shandong Province (no. tsqn201812087), Key R & D Program of Shandong Province (Major innovation project) (2022CXGC020501), Qingchuang Science and Technology Plan Foundation for Colleges and Universities in Shandong Province (no. 2019KJB009), Young Innovative Talents Introduction & Cultivation Program for Colleges and Universities of Shandong Province (granted by Department of Education of Shandong Province, Sub-Title 1: Innovative Research Team of Advanced Energy Equipment, Sub-Title 2: Innovative Research Team of High Performance Integrated Device).

AUTHOR CONTRIBUTIONS

W.H.: Writing – original draft, validation, investigation, methodology, data curation, visualization. Y.Z.: Conceptualization, writing – review, visualization and editing, methodology. L.W.: Writing – review and editing, funding acquisition, validation. W.S.: Writing – review and editing, methodology, investigation. H.C.: Writing – original draft, formal analysis. J.C.: Writing – review and editing, supervision, funding acquisition, conceptualization, validation. A.L.: Writing – review and editing.

DECLARATION OF INTERESTS

The authors declare no competing interests.

Received: October 26, 2023
Revised: February 27, 2024
Accepted: March 13, 2024
Published: March 16, 2024

REFERENCES

1. Galanie, S., Thodey, K., Trenchard, I.J., Filsinger Interrante, M., and Smolke, C.D. (2015). Complete biosynthesis of opioids in yeast. Science *349*, 1095–1100. https://doi.org/10.1126/science.aac9373.
2. Thodey, K., Galanie, S., and Smolke, C.D. (2014). A microbial biomanufacturing platform for natural and semisynthetic opioids. Nat. Chem. Biol. *10*, 837–844. https://doi.org/10.1038/nchembio.1613.
3. Liu, Z., Tyo, K.E.J., Martínez, J.L., Petranovic, D., and Nielsen, J. (2012). Different expression systems for production of recombinant proteins in Saccharomyces cerevisiae. Biotechnol. Bioeng. *109*, 1259–1268. https://doi.org/10.1002/bit.24409.
4. Sitepu, I.R., Garay, L.A., Sestric, R., Levin, D., Block, D.E., German, J.B., and Boundy-Mills, K.L. (2014). Oleaginous yeasts for biodiesel: Current and future trends in biology and production. Biotechnol. Adv. *32*, 1336–1360. https://doi.org/10.1016/j.biotechadv.2014.08.003.
5. Ntaikou, I., Menis, N., Alexandropoulou, M., Antonopoulou, G., and Lyberatos, G. (2018). Valorization of kitchen biowaste for ethanol production via simultaneous saccharification and fermentation using co-cultures of the yeasts Saccharomyces cerevisiae and Pichia stipitis. Bioresour. Technol. *263*, 75–83. https://doi.org/10.1016/j.biortech.2018.04.109.
6. Botstein, D., and Fink, G.R. (2011). Yeast: An Experimental Organism for 21st Century Biology. Genetics *189*, 695–704. https://doi.org/10.1534/genetics.111.130765.
7. Lu, H., Kerkhoven, E.J., and Nielsen, J. (2022). Multiscale models quantifying yeast physiology: towards a whole-cell model. Trends Biotechnol. *40*, 291–305. https://doi.org/10.1016/j.tibtech.2021.06.010.
8. Nielsen, J. (2019). Yeast Systems Biology: Model Organism and Cell Factory. Biotechnol. J. *14*, 1800421. https://doi.org/10.1002/biot.201800421.

9. Hamann, A., Nguyen, A., and Pannier, A.K. (2019). Nucleic acid delivery to mesenchymal stem cells: a review of nonviral methods and applications. J. Biol. Eng. *13*, 7. https://doi.org/10.1186/s13036-019-0140-0.
10. Sharma, D., Arora, S., Singh, J., and Layek, B. (2021). A review of the tortuous path of nonviral gene delivery and recent progress. Int. J. Biol. Macromol. *183*, 2055–2073. https://doi.org/10.1016/j.ijbiomac.2021.05.192.
11. Ramamoorth, M., and Narvekar, A. (2015). Non Viral Vectors in Gene Therapy- An Overview. J. Clin. Diagn. Res. *9*, GE01–GE6. https://doi.org/10.7860/JCDR/2015/10443.5394.
12. Steirteghem, A.C.V., Nagy, Z., Joris, H., Liu, J., Staessen, C., Smitz, J., Wisanto, A., and Devroey, P. (1993). High fertilization and implantation rates after intracytoplasmic sperm injection.
13. Karra, D., and Dahm, R. (2010). Transfection Techniques for Neuronal Cells: Table 1. J. Neurosci. *30*, 6171–6177. https://doi.org/10.1523/JNEUROSCI.0183-10.2010.
14. Wu, P., Chen, H., Jin, R., Weng, T., Ho, J.K., You, C., Zhang, L., Wang, X., and Han, C. (2018). Non-viral gene delivery systems for tissue repair and regeneration. J. Transl. Med. *16*, 29. https://doi.org/10.1186/s12967-018-1402-1.
15. Schenborn, E.T., and Goiffon, V. (2000). DEAE-Dextran Transfection of Mammalian Cultured Cells. Transcr. Factor Protoc. *130*, 147–153.
16. Badazhkova, V.D., Raik, S.V., Polyakov, D.S., Poshina, D.N., and Skorik, Y.A. (2020). Effect of Double Substitution in Cationic Chitosan Derivatives on DNA Transfection Efficiency. Polymers *12*, 1057. https://doi.org/10.3390/polym12051057.
17. Kim, T.K., and Eberwine, J.H. (2010). Mammalian cell transfection: the present and the future. Anal. Bioanal. Chem. *397*, 3173–3178. https://doi.org/10.1007/s00216-010-3821-6.
18. Holmen, S.L., Vanbrocklin, M.W., Eversole, R.R., Stapleton, S.R., and Ginsberg, L.C. (1995). Efficient lipid-mediated transfection of DNA into primary rat hepatocytes. In Vitro Cell. Dev. Biol. Anim. *31*, 347–351. https://doi.org/10.1007/BF02634283.
19. Shi, J., Ma, Y., Zhu, J., Chen, Y., Sun, Y., Yao, Y., Yang, Z., and Xie, J. (2018). A Review on Electroporation-Based Intracellular Delivery. Molecules *23*, 3044. https://doi.org/10.3390/molecules23113044.
20. Pylaev, T., Vanzha, E., Avdeeva, E., Khlebtsov, B., and Khlebtsov, N. (2019). A novel cell transfection platform based on laser optoporation mediated by Au nanostar layers. J. Biophotonics *12*, e201800166. https://doi.org/10.1002/jbio.201800166.
21. A.F. Catara, M. Bar-Joseph, and G. Licciardello, eds. (2019). Citrus Tristeza Virus: Methods and Protocols (Springer). https://doi.org/10.1007/978-1-4939-9558-5.
22. Chi, Z., Xu, Q., and Zhu, L. (2020). A Review of Recent Advances in Robotic Cell Microinjection. IEEE Access *8*, 8520–8532. https://doi.org/10.1109/ACCESS.2020.2964305.
23. Kotnik, T., Rems, L., Tarek, M., and Miklavčič, D. (2019). Membrane Electroporation and Electropermeabilization: Mechanisms and Models. Annu. Rev. Biophys. *48*, 63–91. https://doi.org/10.1146/annurev-biophys-052118-115451.
24. Furuhata, Y., Sakai, A., Murakami, T., Morikawa, M., Nakamura, C., Yoshizumi, T., Fujikura, U., Nishida, K., and Kato, Y. (2019). A method using electroporation for the protein delivery of Cre recombinase into cultured Arabidopsis cells with an intact cell wall. Sci. Rep. *9*, 2163. https://doi.org/10.1038/s41598-018-38119-9.
25. Chang, M.-L., Chen, J.-C., Yeh, C.-T., Chang, M.-Y., Liang, C.-K., Chiu, C.-T., Lin, D.-Y., and Liaw, Y.-F. (2008). Gene Gun Bombardment with DNA-Coated Gold Particles Is a Potential Alternative to Hydrodynamics-Based Transfection for Delivering Genes into Superficial Hepatocytes. Hum. Gene Ther. *19*, 391–395. https://doi.org/10.1089/hum.2007.152.
26. Kimura, Y., and Yanagimachi, R. (1995). Intracytoplasmic Sperm Injection in the Mouse1. Biol. Reprod. *52*, 709–720. https://doi.org/10.1095/biolreprod52.4.709.
27. Shanmugam, M.M., and Santra, T.S. (2016). Microinjection for Single-Cell Analysis. In Essentials of Single-Cell Analysis Series in BioEngineering, F.-G. Tseng and T.S. Santra, eds. (Springer Berlin Heidelberg), pp. 85–129. https://doi.org/10.1007/978-3-662-49118-8_4.
28. Huang, H., Mills, J.K., Lu, C., and Sun, D. (2011). A universal piezo-driven ultrasonic cell microinjection system. Biomed. Microdevices *13*, 743–752. https://doi.org/10.1007/s10544-011-9544-4.
29. Huang, J., Huang, H., Chen, L., Liu, Y., Li, X., Yang, H., Li, Y., and Zhang, L. (2016). Experimental verification of novel two-point supported piezo-driven cell injector. In 2016 IEEE International Conference on Robotics and Biomimetics (ROBIO) (IEEE), pp. 277–282. https://doi.org/10.1109/ROBIO.2016.7866335.
30. Dai, C., Xin, L., Zhang, Z., Shan, G., Wang, T., Zhang, K., Wang, X., Chu, L.-T., Ru, C., and Sun, Y. (2020). Design and Control of a Piezo Drill for Robotic Piezo-Driven Cell Penetration. IEEE Robot. Autom. Lett. *5*, 339–345. https://doi.org/10.1109/LRA.2019.2958734.
31. Liu, Y., Wang, X., Zhao, Q., Zhao, X., and Sun, M. (2020). Robotic Batch Somatic Cell Nuclear Transfer Based on Microfluidic Groove. IEEE Trans. Autom. Sci. Eng. *17*, 2097–2106. https://doi.org/10.1109/TASE.2020.2989760.
32. Levin, D.E. (2005). Cell Wall Integrity Signaling in *Saccharomyces cerevisiae*. Microbiol. Mol. Biol. Rev. *69*, 262–291. https://doi.org/10.1128/MMBR.69.2.262-291.2005.
33. Kollár, R., Reinhold, B.B., Petráková, E., Yeh, H.J., Ashwell, G., Drgonová, J., Kapteyn, J.C., Klis, F.M., and Cabib, E. (1997). Architecture of the Yeast Cell Wall. J. Biol. Chem. *272*, 17762–17775. https://doi.org/10.1074/jbc.272.28.17762.
34. Riveline, D., and Nurse, P. (2009). "Injecting" yeast. Nat. Methods *6*, 513–514. https://doi.org/10.1038/nmeth.1335.
35. Liu, J., Siragam, V., Gong, Z., Chen, J., Fridman, M.D., Leung, C., Lu, Z., Ru, C., Xie, S., Luo, J., et al. (2015). Robotic Adherent Cell Injection for Characterizing Cell–Cell Communication. IEEE Trans. Biomed. Eng. *62*, 119–125. https://doi.org/10.1109/TBME.2014.2342036.
36. Slomka, N., and Gefen, A. (2010). Finite Element Modeling of Cellular Mechanics Experiments. In Cellular and Biomolecular Mechanics and Mechanobiology Studies in Mechanobiology, Tissue Engineering and Biomaterials, A. Gefen, ed. (Springer Berlin Heidelberg), pp. 331–344. https://doi.org/10.1007/8415_2010_31.
37. Trubelja, A., and Bao, G. (2018). Molecular mechanisms of mechanosensing and mechanotransduction in living cells. Extreme Mech. Lett. *20*, 91–98. https://doi.org/10.1016/j.eml.2018.01.011.
38. Ingber, D.E. (1993). Printed in Great Britain © The Company of Biologists Limited (COMMENTARY).
39. Petridou, N.I., Corominas-Murtra, B., Heisenberg, C.-P., and Hannezo, E. (2021). Rigidity percolation uncovers a structural basis for embryonic tissue phase transitions. Cell *184*, 1914–1928.e19. https://doi.org/10.1016/j.cell.2021.02.017.
40. Malik, A.A., Wennberg, B., and Gerlee, P. (2020). The Impact of Elastic Deformations of the Extracellular Matrix on Cell Migration. Bull. Math. Biol. *82*, 49. https://doi.org/10.1007/s11538-020-00721-2.
41. Kulkarni, T., Mukhopadhyay, D., and Bhattacharya, S. (2022). Dynamic alteration of poroelastic attributes as determinant membrane nanorheology for endocytosis of organ specific targeted gold nanoparticles. J. Nanobiotechnol. *20*, 74. https://doi.org/10.1186/s12951-022-01276-1.
42. Hang, J.-T., Kang, Y., Xu, G.-K., and Gao, H. (2021). A hierarchical cellular structural model to unravel the universal power-law rheological behavior of living cells. Nat. Commun. *12*, 6067. https://doi.org/10.1038/s41467-021-26283-y.
43. Arfsten, J., Leupold, S., Bradtmöller, C., Kampen, I., and Kwade, A. (2010). Atomic force microscopy studies on the nanomechanical properties of Saccharomyces cerevisiae. Colloids Surf. B Biointerfaces *79*, 284–290. https://doi.org/10.1016/j.colsurfb.2010.04.011.
44. Schaber, J., Adrover, M.À., Eriksson, E., Pelet, S., Petelenz-Kurdziel, E., Klein, D., Posas, F., Goksör, M., Peter, M., Hohmann, S., and Klipp, E. (2010). Biophysical properties of Saccharomyces cerevisiae and their relationship with HOG pathway activation. Eur. Biophys. J. *39*, 1547–1556. https://doi.org/10.1007/s00249-010-0612-0.
45. Stenson, J. (2009). Investigating the Mechanical Properties of Yeast Cells, p. 377.
46. Yang, C.-C., Ngo, T., and Tran, P. (2015). Influences of weaving architectures on the impact resistance of multi-layer fabrics. Mater. Des. *85*, 282–295. https://doi.org/10.1016/j.matdes.2015.07.014.
47. Brodsky, J.L., and Skach, W.R. (2011). Protein folding and quality control in the endoplasmic reticulum: Recent lessons from yeast and mammalian cell systems. Curr. Opin. Cell Biol. *23*, 464–475. https://doi.org/10.1016/j.ceb.2011.05.004.
48. Schamberger, B., Ziege, R., Anselme, K., Ben Amar, M., Bykowski, M., Castro, A.P.G., Cipitria, A., Coles, R.A., Dimova, R., Eder, M., et al. (2023). Curvature in Biological Systems: Its Quantification, Emergence, and Implications across the Scales. Adv. Mater. *35*, 2206110. https://doi.org/10.1002/adma.202206110.
49. Hu, M., Diggins, P., and Deserno, M. (2013). Determining the bending modulus of a lipid membrane by simulating buckling. J. Chem. Phys. *138*, 214110. https://doi.org/10.1063/1.4808077.
50. Laadhari, A., Saramito, P., Misbah, C., and Székely, G. (2017). Fully implicit methodology

for the dynamics of biomembranes and capillary interfaces by combining the level set and Newton methods. J. Comput. Phys. *343*, 271–299. https://doi.org/10.1016/j.jcp.2017.04.019.

51. Smith, A.E., Zhang, Z., and Thomas, C.R. (2000). Wall material properties of yeast cells: Part 1. Cell measurements and compression experiments. Chem. Eng. Sci. *55*, 2031–2041. https://doi.org/10.1016/S0009-2509(99)00500-X.
52. Ofek, G., Natoli, R.M., and Athanasiou, K.A. (2009). In situ mechanical properties of the chondrocyte cytoplasm and nucleus. J. Biomech. *42*, 873–877. https://doi.org/10.1016/j.jbiomech.2009.01.024.
53. Smith, A.E., Moxham, K.E., and Middelberg, A.P.J. (1998). On uniquely determining cell–wall material properties with the compression experiment. Chem. Eng. Sci. *53*, 3913–3922. https://doi.org/10.1016/S0009-2509(98)00198-5.
54. Shen, S., Zhong, D., Qu, S., and Xiao, R. (2022). A hyperelastic-damage model based on the strain invariants. Extreme Mech. Lett. *52*, 101641.
55. Kasas, S., Stupar, P., and Dietler, G. (2018). AFM contribution to unveil pro- and eukaryotic cell mechanical properties. Semin. Cell Dev. Biol. *73*, 177–187. https://doi.org/10.1016/j.semcdb.2017.08.032.
56. Guimarães, C.F., Gasperini, L., Marques, A.P., and Reis, R.L. (2020). The stiffness of living tissues and its implications for tissue engineering. Nat. Rev. Mater. *5*, 351–370. https://doi.org/10.1038/s41578-019-0169-1.
57. Zhang, T. (2019). Deriving a lattice model for neo-Hookean solids from finite element methods. Extreme Mech. Lett. *26*, 40–45. https://doi.org/10.1016/j.eml.2018.11.007.
58. Tan, Y., Sun, D., Huang, W., and Cheng, S.H. (2008). Mechanical Modeling of Biological Cells in Microinjection. IEEE Trans. NanoBioscience *7*, 257–266. https://doi.org/10.1109/TNB.2008.2011852.
59. Lacouture, Y., and Cousineau, D. (2008). How to use MATLAB to fit the ex-Gaussian and other probability functions to a distribution of response times. Tutor. Quant. Methods Psychol. *4*, 35–45.
60. Kontomaris, S.V., and Malamou, A. (2020). Hertz model or Oliver & Pharr analysis? Tutorial regarding AFM nanoindentation experiments on biological samples. Mater. Res. Express *7*, 033001. https://doi.org/10.1088/2053-1591/ab79ce.
61. Alabd Alhafez, I., Brodyanski, A., Kopnarski, M., and Urbassek, H.M. (2017). Influence of Tip Geometry on Nanoscratching. Tribol. Lett. *65*, 26. https://doi.org/10.1007/s11249-016-0804-6.
62. Chen, J. (2014). Nanobiomechanics of living cells: a review. Interface Focus *4*, 20130055. https://doi.org/10.1098/rsfs.2013.0055.
63. Hanson, L., Lin, Z.C., Xie, C., Cui, Y., and Cui, B. (2012). Characterization of the Cell–Nanopillar Interface by Transmission Electron Microscopy. Nano Lett. *12*, 5815–5820. https://doi.org/10.1021/nl303163y.
64. Smith, A.E., Zhang, Z., Thomas, C.R., Moxham, K.E., and Middelberg, A.P. (2000). The mechanical properties of *Saccharomyces cerevisiae*. Proc. Natl. Acad. Sci. USA *97*, 9871–9874. https://doi.org/10.1073/pnas.97.18.9871.
65. Maurin, B., Barbe, L., Bayle, B., Zanne, P., Gangloff, J., De Mathelin, M., Gangi, A., Soler, L., and Forgione, A. (2004). In Vivo Study Of Forces During Needle Insertions. In Perspective in Image-Guided Surgery (WORLD SCIENTIFIC), pp. 415–422. https://doi.org/10.1142/9789812702678_0056.
66. Simone, C., and Okamura, A.M. (2002). Modeling of needle insertion forces for robot-assisted percutaneous therapy. In Proceedings 2002 IEEE International Conference on Robotics and Automation (Cat. No.02CH37292) (IEEE), pp. 2085–2091. https://doi.org/10.1109/ROBOT.2002.1014848.
67. Tan, Y., Sun, D., Huang, W., and Cheng, S.H. (2010). Characterizing Mechanical Properties of Biological Cells by Microinjection. IEEE Trans. NanoBioscience *9*, 171–180. https://doi.org/10.1109/TNB.2010.2050598.
68. Okamura, A.M., Simone, C., and O'Leary, M.D. (2004). Force Modeling for Needle Insertion Into Soft Tissue. IEEE Trans. Biomed. Eng. *51*, 1707–1716. https://doi.org/10.1109/TBME.2004.831542.
69. Kosoglu, M.A., Hood, R.L., and Rylander, C.G. (2012). Mechanical strengthening of fiberoptic microneedles using an elastomeric support: STRENGTHENING OF FIBEROPTIC MICRONEEDLES. Lasers Surg. Med. *44*, 421–428. https://doi.org/10.1002/lsm.22026.
70. Pryor, R.W. (2009). Multiphysics Modeling Using COMSOL®: A First Principles Approach (Jones & Bartlett Publishers).

STAR★METHODS

KEY RESOURCES TABLE

REAGENT or RESOURCE	SOURCE	IDENTIFIER
Chemicals, peptides, and recombinant proteins		
porous polycarbonate film	Beijing Safelab Technology Co., Ltd.	Databases: CB25778397
Peptone	Angel Yeast Co., Ltd.	Databases: 73049-73-7
Critical commercial assays		
Anton paar NHT^3 Nanoindentation	Measure force-displacement curves	RRID:SCR_024829
Deposited data		
the raw data of nanoindentation	This text	Mendeley Data: https://doi.org/10.17632/22b2ghcfm5.1
puncture model	This text	Mendeley Data: https://doi.org/10.17632/22b2ghcfm5.1
Experimental models: Organisms/strains		
Baker's yeast	Shandong Shengqi Biological Co., Ltd.	Databases: 68876-77-7
Software and algorithms		
COMSOL Multiphysics®(6.0)	Simulation	RRID:SCR_014767
GNU Octave (GUI)	Curve Fitting	RRID:SCR_014398

RESOURCE AVAILABILITY

Lead contact

Further information and requests for resources and reagents should be directed to and will be fulfilled by the lead contact, Jun Chen (chenjun@qlu.edu.cn).

Materials availability

This study did not generate new unique reagents. Requests for resources and reagents should be directed to and will be fulfilled by the lead contact, Jun Chen (chenjun@qlu.edu.cn).

Data and code availability

- Nanoindentation data and puncture model effect video has been uploaded to Mendeley. The dataset is publicly available as of the date of publication. The DOI is listed in the key resources table.
- The original code was written through octave and placed in the supplemental information.
- Any additional information required to reanalyze the data reported in this paper is available from the lead contact upon request

EXPERIMENTAL MODEL AND STUDY PARTICIPANT DETAILS

Microbe strains

We obtained Baker's yeast from Shandong Shengqi Biological Co., Ltd., specific information is available in the key resources table. Yeast cells are stored in our laboratory at 4°C. Yeast cells were cultured in sterile medium containing 200 μL YPD (yeast extract, peptone, glucose medium) at 30°C and 5% CO2 for 48 h. Use a pipette to take 10 μL of culture medium containing yeast cells and place it in 100 μL of phosphate buffer for nanoindentation experiments. Details about exclusion are included in the method details below for each of these experiments.

METHOD DETAILS

Construction of FEA models of yeast cells

The design of microneedle parameters for yeast cells relies primarily on experimental analysis and Finite Element Analysis (FEA). Real-world experiments are complex, involving uncontrollable factors. To address these challenges, constructing yeast cell models aids in understanding the forces and cell morphology during puncturing. These models also assess yeast cell mechanical responses in microinjection scenarios, aiming for realistic representations. The models seek to mimic actual yeast cells, considering factors such as the cell wall's multilayer rigid structure, internal turgor pressure, and mechanical response after puncturing. There are two primary model categories: the tensegrity model and the elastic model. The tensegrity model stabilizes cell structure by integrating compression-resistant elements to counteract global cell

deformation.[38,57] Elastic models have been implemented to calculate Young's modulus at small deformations as well as to simulate cell compression tests at large deformations.[58]

In preparation for constructing a yeast cell microinjection model, a three-dimensional representation of yeast cells was developed (Figure 1A). This model was based on observations of yeast cell morphology under a optical microscope and measurements of their average cell diameter (See Figure S4). Before creating the microinjection model for yeast cells, it is essential to establish theoretical assumptions through analysis.

(1) Yeast cell width (diameter) is generally about 2–6 μm, length of 5–30 μm. Some are longer, and the shape is spherical, oval and columnar, here take the oval for two-dimensional axisymmetric structure modeling.
(2) Assuming uniform thickness before deformation.
(3) The force of dextran on the deformation of the cell wall can be regarded as the uniform mechanical pressure applied.
(4) The gap between the fibers is sufficiently small that the shear stress applied is not much different from that of a gapless shape.

Combining the physiological size and shape of yeast cells under the above premises, we constructed a three-layer ellipsoid axisymmetric structural model, including the cell membrane, cytoplasm, and cell wall. The model has a length of 8 μm and a width of 6 μm (Figure 1C). Yeast cells are not an empty shell structure; the inner cytoplasm, acting as an incompressible liquid, possesses its own osmotic pressure, which increases with cell deformation. In finite element analysis, we applied a spring-based boundary condition to the inside of the ellipsoidal cell membrane, increasing with the depth of indentation to approximate the internal turgor of the cytoplasm and effectively simulate the cytoplasm (See Figure S4). The reported turgor pressure values ranged from 0.1 to 1.0 MPa,[43,44] and the initial intracellular swelling pressure is taken as 0.5 MPa.

Calibration of model parameters

The relationship between cell wall strain and displacement is commonly derived through experimental methods like nanoindentation force-displacement analysis. Young's modulus (E) determination accounts for variations due to cell types and environmental differences. It involves the inverse inference of nanoindentation force-displacement data to calibrate the Young's modulus, often conducted using Octave((GUI))'s fminsearch (SI) function to minimize model error.[59] This process ensures consistency between the model output and force-displacement curves obtained from experiments (See Figure S2). Subsequently, the shear modulus is derived from the classical plate theory, establishing its correlation with Young's modulus. Following this calibration, incorporating the generated Young's and shear moduli alongside distinct cell wall parameters like λ and μ, the yeast cell model undergoes calibration. Once calibrated, the yeast model is utilized to formulate the puncture equation. The parameters of the puncture equation are determined by fitting the force and displacement curves. This process ensures an alignment between the yeast model's output and experimental data, refining the puncture equation parameters for accurate representation.

The relationship between indentation depth (h) and applied load (F) in a conical indenter is typically described by the Hertz and Sneddon models.[60] The Hertz model primarily characterizes the elastic deformation of both the tip (modeled as a spheroid) and the cell (also modeled as a spheroid). Conversely, the Sneddon model is suitable for non-spheroid tips. The concept of an "equivalent cone angle" traditionally aligns the indentation results of the Berkovich triangular pyramid with a cone.[61] The equation establishing the relationship between indentation depth (h) and applied load (F) for a conical indenter is often expressed as follows:[60,62]

$$F = \frac{2}{\pi}\frac{E}{1-v^2}(\tan\theta)h^2, \qquad \text{(Equation 29)}$$

Where E and v are Young's modulus and Poisson's ratio of yeast cells, respectively, and θ is the half-angle of the cone. The shear modulus is expressed as:

$$G = \frac{E}{2(1+v)}, \qquad \text{(Equation 30)}$$

Injection parameter modeling during penetration

Indentation models for yeast cells

The puncture model of yeast cells encompasses three distinct stages throughout the puncturing process: cell wall destruction, cell wall and membrane rupture, and cytoplasm penetration. The force observed throughout these stages is correlated with both stiffness force and cutting force. Considering rupture dynamics, following cell wall rupture, nanoneedles might exhibit close adhesion to the membrane, cause membrane tearing, or recoil away from the membrane,[63] which warrants detailed investigation. However, prior studies exploring the mechanical properties of yeast cell walls revealed experimental curve results indicating simultaneous puncture of the membrane when the cell wall is penetrated.[45,64] Hence, our primary focus lies on investigating the initial puncture stage. Model formulas for constructing the process of puncturing yeast cells, drawing on the experience of building skin,[65] tissues,[66] and other cell puncture models:[67,68]

A linear relationship is assumed between stress $[\sigma_x\sigma_y\sigma_z\tau_x\tau_y\tau_z]^T$ and strain $[\varepsilon_x\sigma_y\varepsilon_z\gamma_x\gamma_y\gamma_z]^T$,

$$\sigma = D\varepsilon = \frac{EG}{(1+v)(1-2v)}, \qquad \text{(Equation 31)}$$

From the generalized Hooke's law and the relationship between isotropic strain and stress, we can know the lame constants λ and μ,

$$\lambda = \frac{Ev}{(1-2v)(1+v)}, \quad \text{(Equation 32)}$$

$$\mu = \frac{E}{1(1+v)} = G, \quad \text{(Equation 33)}$$

And

$$G = \begin{bmatrix} 1-v & v & v & & & \\ v & 1-v & v & & & \\ v & v & 1-v & & & \\ & & & 0.5-v & & \\ & & & & 0.5-v & \\ & & & & & 0.5-v \end{bmatrix}, \quad \text{(Equation 34)}$$

The mesh stiffness matrix K can be obtained,

$$K = \frac{EV}{(1+v)(1-v)} B^T G B, \quad \text{(Equation 35)}$$

where B is the relative position of the element, and V is the volume of the element. Nonlinear strains make the forces dependent on nodal displacements. force is described as

$$F_n = k_{11} u_n + k_{12} u_c + g(u) u_n, \quad \text{(Equation 36)}$$

$$F_c = k_{21} u_n + k_{22} u_c + g(u) u_c, \quad \text{(Equation 37)}$$

where u_n and u_c are the displacements of the uncontacted point and the contact point. F_n and F_c represent contact force and non-contact force. When the microneedle punctures the yeast cell model, it can be predicted by the deformation displacement of any point on the cell. The two-dimensional image is shown in Figure 1E. The equation can be shown as follows:

Contact area:

$$\frac{d\lambda_1}{d\varphi} = -\frac{\lambda_1}{\lambda_2 \sin\varphi}\left(\frac{(T_1 - T_2)\partial\lambda_1}{\partial T_1}\right) - \left(\frac{\lambda_1 - \lambda_2 \cos\theta}{\sin\varphi}\right)\left(\frac{\partial\lambda_1}{\partial\lambda_2}\right), \quad \text{(Equation 38)}$$

$$\frac{d\lambda_2}{d\varphi} = \frac{\lambda_1 - \lambda_2 \cos\theta}{\sin\varphi}, \quad \text{(Equation 39)}$$

Non-contact area:

$$\frac{d\lambda_1}{d\varphi} = \left(\frac{\lambda_2 \sin\varphi \cos\varphi - \omega \sin\varphi}{\sin^2\varphi}\right)\left(\frac{\partial\lambda_1}{\partial\lambda_2}\right) - \left(\frac{d\delta}{\delta d\varphi}\right)\left(\frac{(T_1 - T_2)\partial\lambda_1}{\partial T_1}\right), \quad \text{(Equation 40)}$$

Considering the relationship with intracellular turgor pressure and not considering tip friction, it can be constructed as

$$\int_{x=0}^{x=x_i} F dx = PA, \quad \text{(Equation 41)}$$

$$\frac{d\eta}{d\varphi} = \frac{\cos\theta d\lambda_1}{d\varphi}\frac{z}{\lambda_1} + \left(\frac{\lambda_1{}^2 - z^2}{\delta}\right)\left(\frac{T_2}{T_1}\right) - \left[\frac{\lambda_1(\lambda_1{}^2 - z^2)^{\frac{1}{2}} P h_0}{T_1}\right], \quad \text{(Equation 42)}$$

where P is the cell turgor pressure, x_i is the displacement when the microneedle penetrates into the cell, and A is the contact area between the microneedle and the cell. F is the puncture force, which should meet the following boundary conditions:

$$u_z = u, u_x = u_y = 0, \quad \text{(Equation 43)}$$

$$\varphi = \theta, (\lambda_1)_{contact\ region} = (\lambda_2)_{non-contact\ region}, \quad \text{(Equation 44)}$$

$$\varphi = \theta, \eta' = 0 \text{ or } \delta' = \lambda_1, \quad \text{(Equation 45)}$$

The relationship between force and displacement during the deformation process can be obtained by using the empirical formula:

$$f_{needle}(x) = f_s(x) + f_c(x) =$$

$$(c + b)e^{a(x-d)} + b, 0 \leq x \leq x_d, \quad \text{(Equation 46)}$$

where $f_s(x)$ is a function of the stiffness force and $f_c(x)$ is a function of the cutting force. The model coefficients (a, b, c, and d) are the parameters of the puncture equation in the cell wall destruction stage, and the least squares method is used to fit the obtained indentation curve.

Needle shape

Using a nanoindentation triangular indenter, we investigated needle shape parameters to improve yeast cell puncture efficiency. Our study compared triangular, bullet, and spherical tips and explored conical microneedles with different aspect ratios produced by electrochemical etching. We analyzed cone, sphere, and triangular pyramid tips to design conical needles with varying wall angles and curvatures for precise puncture studies. Through sophisticated finite element simulations, we controlled the puncture speed to unveil stress and strain fields. Our findings underscore the significance of microneedle shape, size, length, tip radius, and wall angle in meeting puncture requirements, minimizing cell damage, and averting bending or breakage (Figure 1C). This analysis aimed to establish optimal needle parameters for efficient yeast cell puncture.

Needle strength

During microneedle penetration of yeast cells, increasing axial force leads to cell penetration once the critical force is reached. If the penetration force exceeds the microneedle's mechanical strength, it may bend or break before penetrating. Blunt or short probes may fail to compensate for wall bending, hindering penetration or causing significant cell deformation and reduced survival. Sharp microneedles lower penetration force, aiding yeast cell puncture but compromising mechanical strength.[69] Using a simplified cantilever beam model for microneedle aspiration analysis (Figure 1D), we calculate the maximum axial pressure according to instability theory combined with the microneedle's structure (See Figure 1).

Model construction in Comsol

The solid mechanics module was utilized to construct a 2D axisymmetric model in Comsol software.[70] Fabrication of conical microneedles and elliptical yeast cells establishes an assembly relationship between them. Graph subtraction is employed to construct yeast cell walls, integrating coupled beams and solid mechanics modules. The beam module utilizes intersecting lines to simulate cellulose cross-linking, and constructs randomly distributed cylinders to mimic glycoprotein distribution (Figure 1B). The microneedle material was set as tungsten, while the yeast cell material was defined as a Neo-Hookean hyperplastic incompressible material with a Young's modulus of 1.95 ± 0.08 *MPa*, a Poisson's ratio of 0.5, and a density of 1.2 g/cm^3. Contact pairs were established between the spherical tip and the yeast model. A steady-state solver was established, with the microneedle model designated as the "source" and the yeast model as the target domain. Utilizing the augmented Lagrange method and segregated solvers, penalty factors were preset to control the fine-tuning option "stability." Typically, contact issues in their initial configuration are unstable. To assist the solver in finding the initial solution, a "spring" was set between contact surfaces, simulating the effect of cellular internal pressure by gradually removing loaded parameters:

$$F_n = k\vartheta \quad \text{(Equation 47)}$$

This linear relationship between force and displacement was established through the penetration value between the contact stiffness (K), contact force (Fn), and re-contact area (ϑ). A parameter (RampFactor) was utilized to introduce a spring base Kz in the z-direction. Specifically,

$$k_z = k_0 * (1 - RampFactor) * 2^{(-\text{RampFactor}*10)}, \quad \text{(Equation 48)}$$

When defining the contact pair, gap and overlap on the gap face were set to zero (assuming no misalignment in reality). Constraints for displacing the rigid microneedle were applied in the x and y directions, set to zero. Utilizing refined mesh division, the mesh on the target boundary of the contact pair was finer than that on the source boundary. In parameter settings, altering the predictor to a constant would stabilize convergence. Parametric scans were applied to the rigid microneedle (ranging from 0 to r). The MUMPS direct solver was utilized for equation resolution. A system of nonlinear equations was solved employing the separation method, with Components set to All and Jacobian format set to Automatic. The Newton-type nonlinear solution method was chosen, with an initial damping coefficient of 1. The termination technique was set to iteration or tolerance, with 7 iterations and a tolerance factor of 1. Additionally, a time step growth limit of 1 was imposed, and an adaptive grid method was adopted. Simultaneously, a global parameter, "Indentation," was introduced, with values ranging from 0 to 1 incremented by 0.1 at intervals. Auxiliary scanning was employed to facilitate research expansion.

Preparation of yeast cells

Preparation of yeast cell suspension: 2 g of dried yeast (Baker's yeast, Shandong Shengqi Biological Co., Ltd.), 2 g of peptone (Angel Yeast Peptone FP103, Angel Yeast Co., Ltd.) dissolved in 90 mL sterile water and added 10 mL of glucose solution was configured into a cell

suspension, and cultured at 25°C for 24 h to obtain a stable reproducible cell suspension. During the test, the solution was heated to room temperature, 1 to 2 mL of the solution was filtered using a porous polycarbonate film (pore size of 2–5 μm) to fix yeast cells, and the porous polycarbonate film (Beijing Safelab Technology Co., Ltd.) adhered to yeast cells was fixed to the coverslip with double-sided tape, and the resulting coverslip was used for nanoindentation experiments.

Calculating the cell area in optical microscopy image

Image processing is mainly divided into four steps (see Figure S5). Convert RBG image to 8-bit grayscale image (Image > Type > 8-bit). Select the appropriate threshold to adjust the image, and then Apply to get the binarized image (Image > Adjust > Threshold). Use the watershed function to automatically segment the cells of the image, and use brushes to supplement the contour edges (Process > Binary > Watershed). Set ruler and use 'Analyze Particles' to obtain cell data. Set the lower limit of Size to filter out some small noise (Analyze > Analyze Particles).

Indentation of yeast cells

A polycarbonate film with a pore size of 4 μm was mounted onto a glass slide to fix the yeast cells during optical observation. Utilizing a nano-indenter (Figure 2B) (Anton Paar NHT^3 Nano-indenter with a Poisson ratio vi of 0.07, Young's modulus (Ei) of 1140 GPa, and shear modulus (G) of 398 GPa), the probe was meticulously brought into contact with the cell surface to determine the contact point. The experiment employed a three-stage loading curve—consisting of loading, load holding, and unloading—operating in static load control mode with a set Poisson's ratio (λ) of 0.5. A Berkovich tapered diamond tip was used, focusing on a 3x3 test area to balance statistical significance while minimizing cellular interference. Within this area, ten indentation points were randomly chosen for assessment. The loading load was standardized at 250 μN, with loading and unloading times both set to 30 s, maintaining a load unloading of 90% to mitigate thermal drift. To minimize the impact of creep on results, a 10-s holding time was implemented. Real-time monitoring of force-displacement curves during indentation facilitated the analysis of the relationship between the force and displacement of the indenter.

QUANTIFICATION AND STATISTICAL ANALYSIS

Use OriginLab 2021 version software to perform statistical analysis on the data. Numerical results are expressed as mean ± SEM (see Figure 2D). Quantitative data in line charts and individual data points are presented as averages (Figures 3 and 4). Statistical analyses were performed using two-tailed unpaired Student's t-tests. $p < 0.05$ was the criterion for statistically significant group differences.